

# Core–Shell MOF-in-MOF Nanopore Bifunctional Host of Electrolyte for High-Performance Solid-State Lithium Batteries

Ahmed Eissa Abdelmaoula, Jun Shu, Yu Cheng, Lin Xu,\* Gang Zhang, Yangyang Xia, Muhammad Tahir, Peijie Wu, and Liqiang Mai\*

Solid-state lithium-ion batteries with high safety are the encouraging next-generation rechargeable electrochemical energy storage devices. Yet, low  $\text{Li}^+$  conductivity of solid electrolyte and instability of solid–solid interface are the key issues hampering the practicability of the solid electrolyte. In this research, core–shell MOF-in-MOF nanopores UIO-66@67 are proposed as a unique bifunctional host of ionic liquid (IL) to fabricate core–shell ionic liquid–solid electrolyte (CSIL). In the current design of CSIL, the shell structure (UIO-67) has a large pore size and a high specific surface area, boosting the absorption amount of ionic liquid electrolyte, thus increasing the ionic conductivity. Nevertheless, the core structure (UIO-66) has a small pore size compared to the ionic liquid, which can confine the large ions, decreasing their mobility, and selectively boost the transport of  $\text{Li}^+$ . The CSIL solid electrolyte exhibits considerable enhancement in the lithium transference number ( $t_{\text{Li}^+}$ ) and ionic conductivity compared to the homogenous porous host (pure UIO-66 and UIO-67). Additionally, the Li|CSIL|Li symmetric batteries maintain a stable polarization of less than 28 mV for more than 1000 h at  $1000 \mu\text{A cm}^{-2}$ . Overall, the results demonstrate the concept of core–shell MOF-in-MOF nanopores as a promising bifunctional host of electrolytes for solid-state or quasi-solid-state rechargeable batteries.

## 1. Introduction

Presently, there is a growing requirement for rechargeable batteries for electric vehicles and smart electronics.<sup>[1–3]</sup> Lithium-ion batteries (LiBs) with IL provide a promising solution of the problems of flammable organic liquid electrolyte, owing to the advantages of nonvolatile, nonflammable, and high ionic conductivity. However, the drawbacks of IL are low  $t_{\text{Li}^+}$  with limited lithium-ion diffusion within the electrolyte and electrode/electrolyte interfaces, low stability against electrodes, and poor impregnation of the separator.<sup>[4]</sup> These problems hinder the practical application of IL for batteries.

Recently, solid electrolyte instead of flammable organic liquid electrolyte, and IL electrolyte have been broadly exploited in next-generation rechargeable electrochemical energy storage devices, owing to high safety, long cycle life, and mature technologies.<sup>[5–8]</sup> However, the funda-

mental issues hampering the viability of solid electrolytes can be illustrated according to the type of solid electrolyte.<sup>[9–14]</sup> Generally, polymer electrolyte has low ionic conductivity at room temperature ( $10^{-7}$  to  $10^{-6}$  S  $\text{cm}^{-1}$ ).<sup>[15,16]</sup> On the contrary, ceramic electrolyte exhibits a high ionic conductivity ( $10^{-4}$  to  $10^{-2}$  S  $\text{cm}^{-1}$ ) at room temperature,<sup>[17]</sup> but still has a poor interface with electrodes.


Meanwhile, to boost the performance of solid electrolytes, the most intriguing strategies focused on achieving high electrochemical stability against electrodes, low interfacial resistance, and high ionic conductivity.<sup>[18–24]</sup> Accordingly, tremendous techniques have been utilized to enhance the performance of solid electrolytes, such as polymer blend,<sup>[25]</sup> ionic liquid incorporation,<sup>[26]</sup> grafting short oligomers onto the polymer backbone,<sup>[27]</sup> and introducing inorganic fillers.<sup>[28–30]</sup> Nevertheless, unsatisfactory electrochemical stability and massive interfacial resistance are significant challenges hindering the practical use of solid electrolytes in solid-state lithium-ion batteries.

To overcome the above challenges, porous nanostructures could be utilized as a host to load minor ionic liquid to accomplish a stable solid electrolyte with high ionic conductivity.

A. E. Abdelmaoula, J. Shu, Y. Cheng, Prof. L. Xu, G. Zhang, Y. Xia, Dr. M. Tahir, P. Wu, Prof. L. Mai  
State Key Laboratory of Advanced Technology  
for Materials Synthesis and Processing  
School of Materials Science and Engineering  
Wuhan University of Technology  
Wuhan 430070, China  
E-mail: linxu@whut.edu.cn; mlq518@whut.edu.cn

A. E. Abdelmaoula  
Mining and Metallurgical Department  
Faculty of Engineering  
Al-Azhar University  
Cairo 11884, Egypt

Prof. L. Xu, Prof. L. Mai  
Foshan Xianhu Laboratory of the Advanced Energy Science  
and Technology Guangdong Laboratory  
Xianhu hydrogen Valley  
Foshan 528200, China

 The ORCID identification number(s) for the author(s) of this article can be found under <https://doi.org/10.1002/smt.202100508>.

DOI: 10.1002/smt.202100508

Recently, new exciting structures have been depicted in the literature; specifically, metal-organic frameworks (MOFs), that were intensively investigated as one of the fascinating class of porous materials. The MOFs are widely used in industrial<sup>[31–36]</sup> and energy storage applications such as anode<sup>[37–40]</sup> and cathode.<sup>[41–43]</sup>

Currently, the practicability of MOFs as solid electrolytes in LiBs has received extensive attention due to the following: MOFs with high specific surface area and small pore size can further strengthen the effect of anion absorption and firmly trap anions around the surface, leading to a high  $t_{\text{Li}^+}$ . Physico-chemical properties of MOF, such as mechanical and electrochemical stabilities can maintain stable Li plating/stripping and decrease electrode/electrolyte interfacial resistance. In addition, due to poor electrical conductivity, permanent porosity, and controllable morphology, MOFs can work as excellent platforms for building ionic conductors and improve the transport of ions.<sup>[44–47]</sup>

Different MOFs with various pore sizes and specific surface areas have been utilized as solid electrolytes.<sup>[48–52]</sup> The MOF materials with large pore size and high specific surface area like UIO-67 could load sufficient ionic liquid, which exhibit high ionic conductivity but still hampered by its low  $t_{\text{Li}^+}$  due to large pore size.<sup>[52]</sup> By contrast, other MOF materials with small pore size comparable to the IL like UIO-66 and MOF-525(Cu) highly confine the large ions and selectively improve the transport of  $\text{Li}^+$ . However, the low specific surface area and small pore size decrease the absorption amount of ionic liquid, which leads to low ionic conductivity.<sup>[53,54]</sup> Given that each pure MOF has its benefits and drawbacks, it is strenuous to find a single MOF with a homogeneous structure to increase ionic conductivity and enhance selective transport of lithium-ions concurrently. To overcome the previous challenges, heterogeneous MOF-in-MOF structures are used here to improve the ionic conductivity and enhance the selective transport of lithium-ions. In our current design, the shell structure (UIO-67) has a large pore size and high specific surface area, which can increase the absorption amount of IL electrolyte. On the other hand, the core structure (UIO-66) has a small pore size comparable to the IL ions, which highly confines these large ions and selectively enhances the transport of  $\text{Li}^+$ . In addition, porous structure with sphere nanoparticles of core-shell MOF-in-MOF host can provide a stable 3D open solid framework. The adjacent framework channels can provide a stable conductive pathway throughout the electrolyte and electrolyte/electrode interface. Thus, our designed MOF-in-MOF structures can achieve both high ionic conductivity and high  $t_{\text{Li}^+}$  simultaneously, which is hardly achieved by pure MOFs and IL.

From the survey, it can be deduced that the  $\text{H}_2\text{-bpydc}$  was utilized as a linker to fabricate the shell structure of UIO-66@67 in catalytic carboxylation application. Herein, we used  $\text{H}_2\text{-bpdc}$  as a linker for the first time to fabricate core-shell MOF-in-MOF nanopores UIO-66@67, which can diminish the cost by about 100 times, making it suitable for several applications, and enlarging its probability in utilizing practically in the battery applications. Meanwhile, according to the available data, no study that has utilized the MOF core-shell structure as host of electrolyte in solid-state batteries. Therefore, to fill

this research gap, the current study aims to examine the UIO-66@67 as a unique bifunctional host of electrolyte to enhance ionic conductivity,  $t_{\text{Li}^+}$ , and interface stability of solid electrolyte. Moreover, the assembled Li/LFP cell based on CSIL solid electrolyte exhibits outstanding specific charge/discharge capacity of  $158 \text{ mAh g}^{-1}$ , high Coulombic efficiency after 100 cycles with an excellent capacity retention of 99% at  $25^\circ\text{C}$ .

## 2. Results and Discussion

The core-shell MOF-in-MOF nanopores UIO-66@67 with heterogeneous pore sizes were designed, as illustrated in **Figure 1a**. The synthesis of UIO-66@67 using Zr as metal sets with different organic ligands (1,4-benzene dicarboxylic acid (BDC) and biphenyl-4,4-dicarboxylic acid (BPDC)) was constructed for the first time. Synthesis of UIO-66@67 structure was carried out in two steps.

Briefly, Zr clusters connected with BDC linker produced UIO-66 as a core structure followed by the second ligand (BPDC) assemblage to fabricate UIO-67 as a shell structure. The synthesized UIO-66@67 were verified by transmission electron microscopy (TEM) and scanning electron microscopy (SEM) images ascribed to the various shapes and contrast of nanoparticles. From SEM images, the synthesis of UIO-66 and UIO-67 resulted in cubic and octahedral shapes, respectively, with particle size  $\approx 100 \text{ nm}$  (Figure S1a,b, Supporting Information). Whereas the UIO-66@67 structure resulted in a spherical shape having a particle size  $\approx 150 \text{ nm}$  (Figure S1c, Supporting Information). The core-shell structure was also identified by TEM images owing to the discrepancy in shape and contrast of core and shell structure (Figure S1d, Supporting Information). Additionally, x-ray diffraction analysis (XRD) of the synthesized UIO-66@67 confirms that the patterns of UIO-67 and UIO-66 crystal structures are indicated (Figure S2a, Supporting Information).

Fourier transform infrared spectroscopy (FTIR) analysis (Figure S2b, Supporting Information) confirms the presence of coordination between metal sets and linkers in MOF structure through the bridges. That ascribed to the deprotonation of linkers, which is verified by the evanescence of the  $\text{OH}^-$  stretching vibrations from the organic ligands between  $2500$  and  $3000 \text{ cm}^{-1}$ . Moreover, comparing with the vibration of original linkers, a significant shift in stretching vibration of  $\text{C}=\text{O}$  at  $1680 \text{ cm}^{-1}$  in the MOFs result is detected. Eventually, based on SEM, TEM, XRD, and FT-IR analyses, UIO-67 was successfully grown on UIO-66 to produce UIO-66@67 with particle size  $\approx 150 \text{ nm}$ . The UIO-66@67 show a high surface area of  $1970 \text{ m}^2 \text{ g}^{-1}$  which comparable with UIO-67 ( $2050 \text{ m}^2 \text{ g}^{-1}$ ) and higher than UIO-66 ( $1400 \text{ m}^2 \text{ g}^{-1}$ ) (Figure S2c, Supporting Information), which enlarges the absorption amount of ionic liquid. In addition, the reduction in the surface area of UIO-66@67 up to  $10 \text{ m}^2 \text{ g}^{-1}$  indicates the incorporation of Li-IL into the UIO-66@67 pore channels (Figure S2c, Supporting Information). The statistical particle size distribution of UIO-66 and UIO-67 (Figure S2d, Supporting Information), indicating the pore size of UIO-66 is more comparable with the size of ionic liquid than UIO-67. Photograph, SEM images (Figure S3a,b, Supporting Information), and XRD patterns

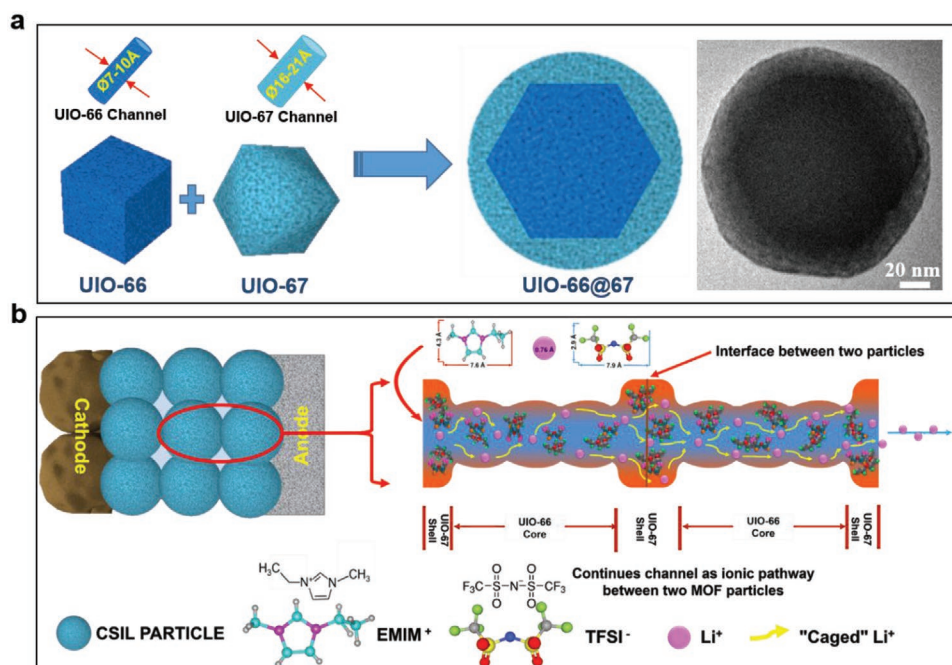


**Figure 1.** a) Schematic diagram of the architecture design of UIO-66@67 with pore size displayed separately and corresponding TEM image. b) Schematic diagram of continued channel (ionic pathway) within the adjacent particles of CSIL and nanowetted interfacial mechanism of the solid electrolyte with a zoom view of transference of Li<sup>+</sup> and confinement of [EMIM]<sup>+</sup> and [TFSI]<sup>-</sup> by UIO-66 pore channel.

(Figure S3c, Supporting Information) of the CSIL electrolyte reveal an insignificant change in shape and crystal structure. This is ascribed to incorporating Li-IL and pressing under 30 MPa, demonstrating the high chemical and mechanical stability of solid electrolyte. In order to observe the thermal stability of the UIO-66@67, thermogravimetric analysis (TGA) was conducted (Figure S3d, Supporting Information); the weight loss at 180 °C is ascribed to the solvent evaporated from the pores. Additionally, the UIO-66@67 maintain high thermal stability (up to 550 °C) compared to UIO-66. The TGA analysis of CSIL solid electrolyte indicates a high degradation temperature over 360 °C (Figure S3d, Supporting Information). Given the excellent thermal stability of the current CSIL solid electrolyte, it is expected to work at low and high temperatures in LiBs.

A solid-state battery with CSIL solid electrolyte was created, and its operating mechanism is demonstrated in Figure 1b. The ionic conductivity is a crucial and essential factor of solid electrolytes in LiBs. The amount of Li-IL in the CSIL solid electrolyte was optimized before other electrochemical tests to determine the appropriate amount of Li-IL, which achieves higher ionic conductivity. Different amount of Li-IL was mixed with activated UIO-66@67, and then they were pressed into pellets with 160 μm thickness under 10 MPa. The distribution of S and F elements in CSIL was demonstrated by energy dispersive x-ray spectroscopy (EDS) (Figure S4, Supporting Information), indicating that the Li-IL is uniformly distributed in UIO-66@67, and enhanced the ionic conductivity. Electrochemical impedance spectroscopy (EIS) characterization of solid electrolytes with different amounts of Li-IL and pristine Li-IL was performed at room temperature (Figure S5a, Supporting Information). It is evident that the ionic conductivity increases with

the content of Li-IL. Apparently, the ionic conductivity of pristine Li-IL is  $6.5 \times 10^{-3} \text{ S cm}^{-1}$ , which is higher than CSIL due to the high amount of Li-IL ions. The CSIL solid electrolyte with Li-IL content more than 1.2 mL displays high ionic conductivity, more than  $2.1 \times 10^{-3} \text{ S cm}^{-1}$ . However, from the sample appearance, it is clear that the IL is not completely absorbed by the UIO-66@67 host, which makes it susceptible to liquid leakage during operation.

On the contrary, the electrolyte with Li-IL less than 1.2 mL appeared as dry powder with complete absorption of Li-IL, which could prevent the risk of leakage during operation and maintain high ionic conductivity reach  $2.1 \times 10^{-3} \text{ S cm}^{-1}$ . Similarly, the impact of temperature on the conductivity of the CSIL solid electrolyte was examined (Figure S5b, Supporting Information). It is evident that the ionic conductivity escalations with increasing the temperature, which gives an initial impression about the thermal stability of the CSIL solid electrolytes in LiBs under a wide range of temperatures. The X-ray photoelectron spectroscopy (XPS) characterization indicates a strong Zr(II) peak with comparatively high intensity in the samples with Li-IL content from 0.6 to 1.2 mL, implying that there is the complete absorption of Li-IL by these samples (Figure S6, Supporting Information). Based on the above results, it can be concluded that the optimum ratio for further experiments is 1.2 g UIO-66@67 to 1.2 mL Li-IL, which exhibited high ionic conductivity ( $2.1 \times 10^{-3} \text{ S cm}^{-1}$ ) and low activation energy (0.086 eV) (Figure S8a,b, Supporting Information). The ionic conductivity of CSIL solid electrolyte is high compared to synthesized UIO-66/Li-IL ( $4.2 \times 10^{-4} \text{ S cm}^{-1}$ ), UIO-67/Li-IL ( $5.8 \times 10^{-4} \text{ S cm}^{-1}$ ) (Figure 2a,b), and even higher than the recently reported works (Figure 2c) and (Table S1, Supporting Information).

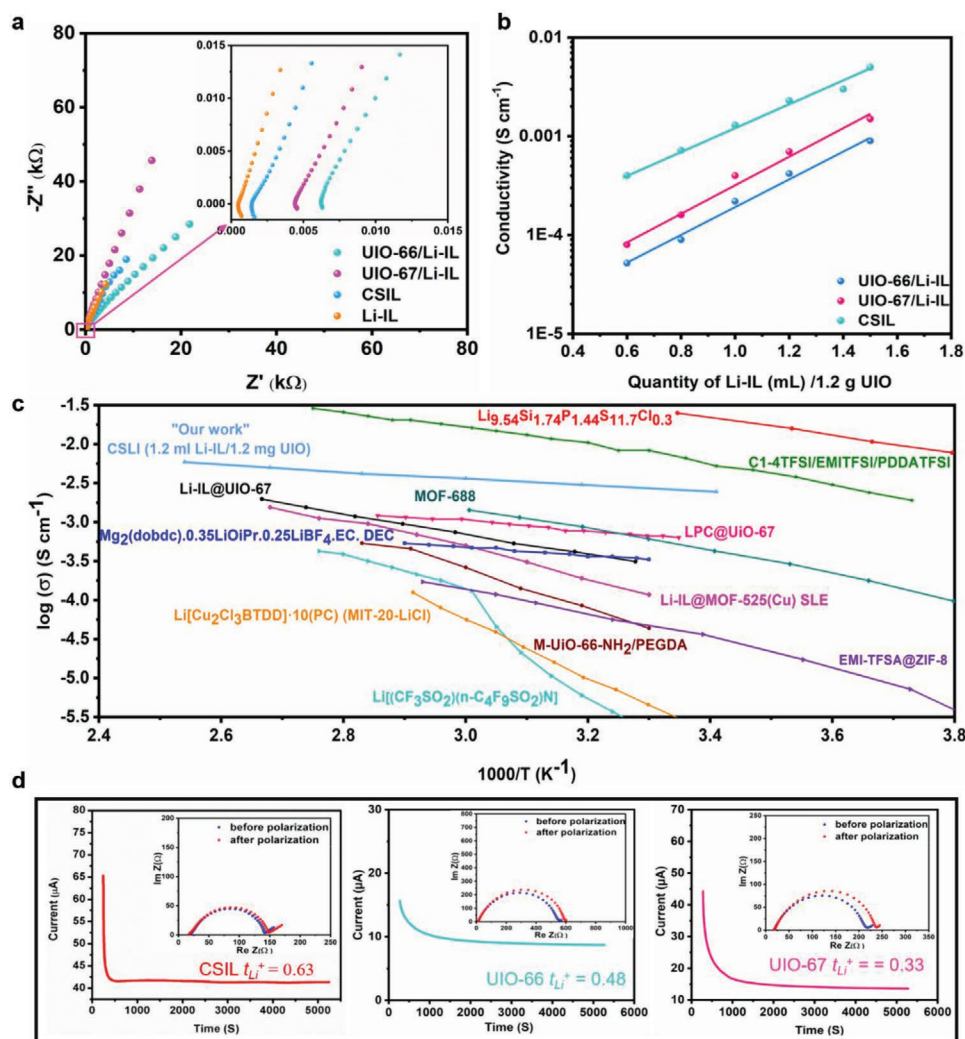


**Figure 2.** Electrochemical characterization of UIO-based solid electrolyte. a) Comparison between AC impedance spectra of Li-IL, UIO-66/Li-IL, UIO-67/Li-IL and CSIL solid electrolytes at room temperature and 1.2 mL Li-IL/1.2 g UIO. b) Arrhenius plots of nanostructured UIO-66, UIO-67 and CSIL solid electrolyte with different compositions at room temperature. c) Comparison of Arrhenius plots of CSIL (blue) with other reported electrolytes such as super ionic conductor ( $\text{Li}_{9.54}\text{Si}_{1.74}\text{P}_{1.44}\text{S}_{11.7}\text{Cl}_{0.3}$ ),<sup>[21]</sup> Organic liquid in solid (LPC@UIO-67,<sup>[48]</sup>  $\text{Mg}_2(\text{dobdc})\cdot 0.35\text{LiO}i\text{Pr}\cdot 0.25\text{LiBF}_4\cdot \text{EC}\cdot \text{DEC}$ )<sup>[49]</sup>, ionic liquid in solid (Li-IL@UIO-67,<sup>[52]</sup> Li-IL@MOF-525(Cu) SLE,<sup>[52]</sup> EMI-TFSA@ZIF-8<sup>[55]</sup>), polymeric electrolyte ( $\text{Li}(\text{CF}_3\text{SO}_2)_n\text{-C}_4\text{F}_9\text{SO}_2\text{N}$ ),<sup>[56]</sup> C1-4TFSI/EMITFSI/PDDATFSI,<sup>[57]</sup> M-UIO-66-NH<sub>2</sub>/PEGDA,<sup>[58]</sup> MOF-688<sup>[59]</sup>, and single ion conductor solid electrolyte  $\text{LiCu}_2\text{Cl}_3\text{BTDD}\cdot 10(\text{PC})$  (MIT-20-LiCl).<sup>[60]</sup> d) DC polarization curve of CSIL, UIO-66/Li-IL and UIO-67/Li-IL solid electrolyte with 1.2 mL of Li-IL at room temperature.

The high ionic conductivity of CSIL solid electrolytes is due to the following reasons. First, during pressing of CSIL into a dense pellet, the UIO-66@67 is packed together in a way that the adjacent framework channels are connected with each other through the nanowetted interface to provide a stable 3D conductive pathway throughout the electrolyte and electrolyte/electrode interface, resulting in an enhanced ionic conductivity, and reduced the resistance of solid electrolyte. The nanowetted interfaces can be noted by XPS (Figure S7, supporting information), which gives torrential information about the contact face (4–6 nm) of the CSIL nanocrystals. The size of shell pore channels is 1.6–2.1 nm (Figure S2d, supporting information). Based on the above and during pressing of CSIL into a dense pellet, the UIO-66@67 particles are packed together at many points in a way that the adjacent framework channels are connected with each other through the contact face (nanowetted

interface). Additionally, strong signals of F and S were observed in the samples with complete impregnation of Li-IL, indicating that Li-IL ions are occupied near the surface of UIO-66@67 nanocrystals, and suggest the formation of nanowetted interface between the MOF nanoparticles (Figure S7, Supporting Information). Second, the high surface area and large pore size of the shell structure (UIO-67) increase the dissolution amount of ionic liquid, enhancing the conductivity of CSIL solid electrolyte.

The electrochemical stability window (ESW) is a fundamental characteristic that defines the durability and the output energy of a battery. To determine the electrochemical stability of CSIL solid electrolyte toward anodic oxidation and cathodic reduction reactions, Li/CSIL/SS asymmetric cell was used to measure the linear sweep voltammetry (LSV) at room temperature (Figure S9, Supporting Information). The CSIL electrolyte



shows a stable electrochemical window up to 5.2 V, owing to the high stability of UIO-66@67 hosts against Li metal.

The  $t_{\text{Li}^+}$  of pristine Li-IL with a glass fiber separator is 0.15 (Figure S10, Supporting Information), and the transport of lithium ions is low because both negative and positive ions move freely. In addition, the majority of the ionic conductive species in Li-IL are  $[\text{EMIM}]^+$  and  $[\text{TFSI}]^-$  rather than  $\text{Li}^+$ . While the  $t_{\text{Li}^+}$  of CSIL solid electrolyte by DC polarization curve at room temperature is 0.63, which is higher than previous reported electrolytes such as Li-IL electrolyte (0.14),<sup>[52]</sup> Li-IL@UIO-67 (0.13),<sup>[53]</sup> Li-IL@UIO-66 (0.33),<sup>[54]</sup> and calculated Li-IL@UIO-67 (0.3), Li-IL@UIO-66 (0.48) by this work (Figure 2d). The high  $t_{\text{Li}^+}$  is accredited to I) the confinement of ionic liquid ions by core host (UIO-66), owing to the comparable size of UIO-66 pore size (8 Å) with ionic liquid ions ( $[\text{EMIM}]^+ \approx 79$  Å and  $[\text{TFSI}]^- \approx 76$  Å),<sup>[61]</sup> while the effect of  $\text{Li}^+$  movement is less due to its small size of 0.76 Å (Figure S11, Supporting Information); II) the high surface area with tightly packed, CSIL sphere nanoparticle crystals can work as excellent platforms for building ionic conductors and improve the transport of ions through the face-sharing among open porous frameworks from one crystal to another.

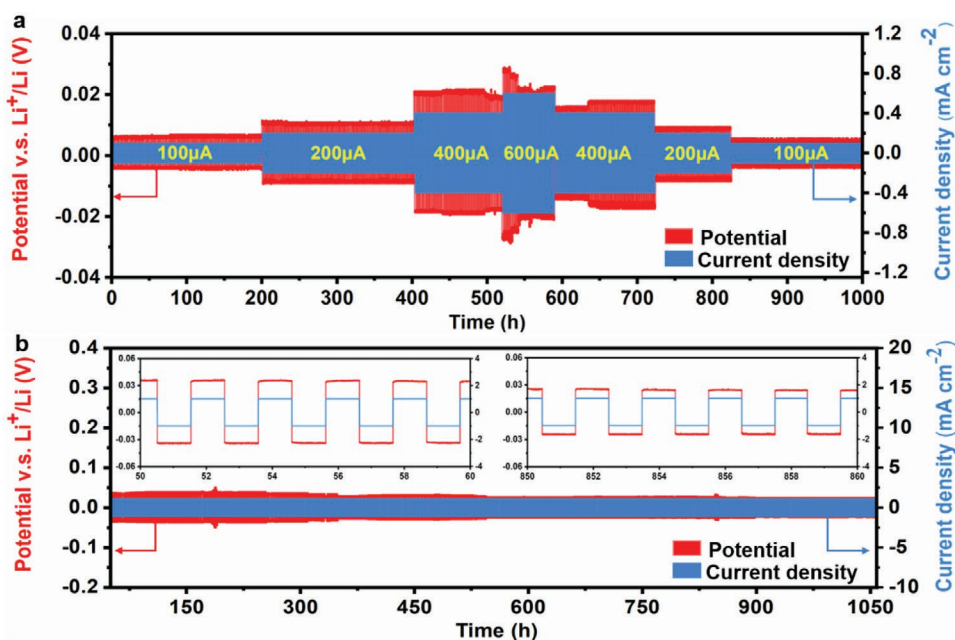
To determine the mechanical stability of CSIL solid electrolyte and lifetime of lithium batteries, long-term electrochemical stability of CSIL electrolyte against Li metal was further measured by symmetric (Li/CSIL/Li) cells. The cell was run for 2 h/cycle under the current densities of 100, 200, 400, and 600  $\mu\text{A cm}^{-2}$  at room temperature (Figure 3a), which maintains a small polarization voltage  $\pm 5, 10, 18,$  and 22 mV, respectively, and remained stable and smooth for over 1000 h.

Figure 3b and S12a (Supporting Information) displays a long-term cycling stability at 1000 and 400  $\mu\text{A cm}^{-2}$  for more than 1000 and 1500 h, respectively. Furthermore, the calculated

resistance based on Ohm's law approximately equals 50  $\Omega \text{ cm}^{-2}$ , which is in good agreement with the AC impedance of CSIL solid electrolyte before and after cycling at 1000  $\mu\text{A cm}^{-2}$  (Figure S13, Supporting Information). The excellent stability is credited to the fast diffusion of  $\text{Li}^+$  in the CSIL solid electrolyte. An additional reason might be attributed to the uniform distribution of  $\text{Li}^+$  on the Li metal electrode surface. From the above results, the CSIL can be applied safely at a wide range of current density (100–1000  $\mu\text{A cm}^{-2}$ ), which is a remarkable value for a solid electrolyte system operating at room temperature (Figure S12b, Supporting Information) displays that the CSIL solid electrolyte possesses minimum polarization voltage (10 mV) compared to UIO-66 (50 mV) and UIO-67 (65 mV) solid electrolytes at 200  $\mu\text{A cm}^{-2}$ .

The results indicate that the CSIL solid electrolyte is more stable compared to UIO-66 and UIO-67 electrolytes reported in this work and other recently reported MOFs based electrolytes (Table S2, Supporting Information).

Finally, to confirm the potential utility of the nanostructured CSIL solid electrolyte in LiBs, prototype solid-state LiBs were assembled to test their specific capacity and cycling stability by employing Li metal foil as an anode, coupled with  $\text{LiFePO}_4$  (LFP) active materials as a cathode and CSIL solid electrolyte (Li/CSIL/LFP). In order to optimize the structure of the cathode which achieve high capacity, excellent Coulombic efficiency, and minimum polarization, charge–discharge curves of cells (Li/CSIL/LFP) were performed based on the composition of the cathode as illustrated in (Figure S14, Supporting Information). The corresponding discharge capacities were obtained as 162, 158, 144, 130, 118, and 108  $\text{mAh g}^{-1}$  at 0.2C and 25 °C. Based on the results given above, it can be clearly that the optimum ratio for further experiments is 6:6:2. Figure 4a,b shows the specific capacity of Li/CSIL/LFP batteries at different rates of 0.2, 0.4,



**Figure 3.** a) Voltage profile of the Li/CSIL/Li symmetric batteries at different current densities (100 200, 400, and 600  $\mu\text{A cm}^{-2}$ ). b) Voltage profile of the Li/CSIL/Li symmetric battery at a current density of 1000  $\mu\text{A cm}^{-2}$  Insets: Detailed voltage profiles of the 50–60 and 850–860 h, respectively. All tests were performed at room temperature.

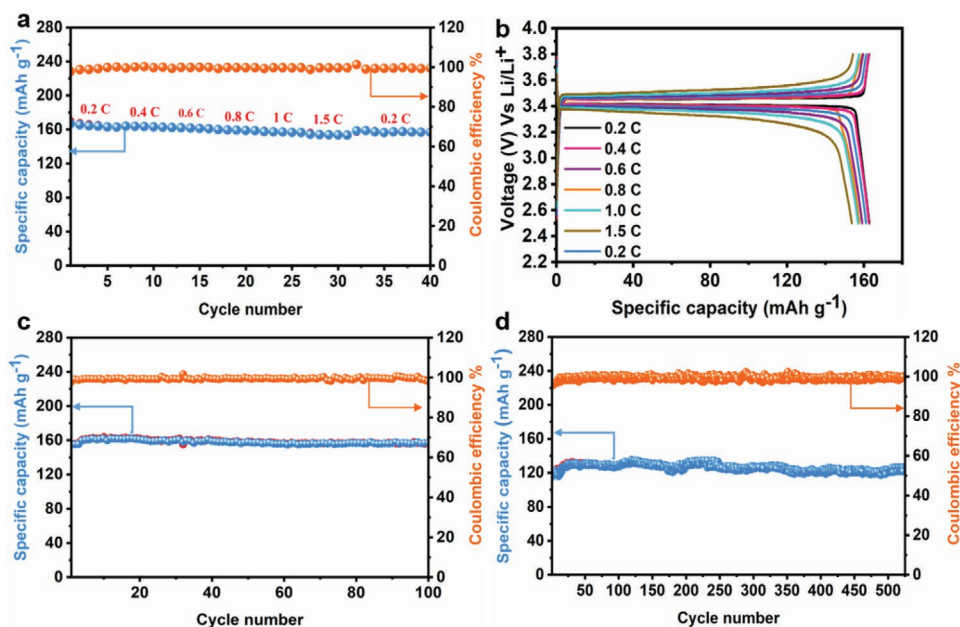


**Figure 4.** Electrochemical performances of Li/CSIL/LFP solid-state batteries. a) Cycling stability with Coulombic efficiency under different current rates 0.2, 0.4, 0.6, 0.8, 1.0, 1.5, and 0.2 C. b) Typical charge/discharge profiles at different current rates. c, d) Cycling stability with Coulombic efficiency under 0.2 and 3 C. All tests were conducted at room temperature.

0.6, 0.8, 1.0, 1.5, and 0.2 C at 25 °C for 40 cycles, which exhibit excellent charge and discharge capacities reaching 163.8, 163.6, 162.3, 160.8, 159, 156, and 162.6 mAh g<sup>-1</sup>, respectively, without noticeable change. Furthermore, it demonstrates a flat operating voltage plateau during charge and discharge cycles (3.455 and 3.40 V respectively), signifying a very small polarization of 0.055 V (Figure 4b) at 0.2 C. In addition, the cycling performance of lithium-ion batteries with CSIL solid electrolyte at 0.1, 2, 3, 4, 5, and 0.1 C were investigated to explore the stability at high current densities (Figure S15a, Supporting Information). It shows that the batteries maintain high capacity and stability at high current density compared to Li-IL (Figure S15b, Supporting Information) with the capacity drop for Li-IL cell at C-rates exceeding 1C, indicating limiting Li<sup>+</sup> diffusion within the electrolyte and the electrode/electrolyte interfaces previously observed elsewhere.<sup>[4]</sup> Figure 4c and Figure S16 (Supporting Information) display the cycling stability and Coulombic efficiency of Li/CSIL/LFP and Li/IL/LFP cells under 0.2C and 25 °C. The batteries with CSIL solid electrolyte show the excellent specific charge/discharge capacity of 158 mAh g<sup>-1</sup> for the cathode, high Coulombic efficiency with an excellent capacity retention of 99% after 100 cycles. In comparison, the batteries with Li-IL electrolyte provides charge/discharge capacity of 159 mAh g<sup>-1</sup> with low-capacity retention of 80%. The failure of IL cell after 98 cycles can be attributed to an internal short circuit due to dendrite growth. In addition, the capacity of CSIL cell is higher than other works related to pure MOF electrolytes,<sup>[47,53,62]</sup> that can be ascribed to the high ionic conductivity, electrochemical stability, interfacial stability, and increased Li<sup>+</sup> transference number. Also from Figure 4c it can be signaled that the capacity of the battery increases slightly before stabilizing due to an enhanced interface (contact) between CSIL solid electrolyte and electrodes and also attributed to the

uniform distribution of Li<sup>+</sup> on the Li metal electrode surface (Figure S17, Supporting Information). Compared with pristine lithium (Figure S17a, Supporting Information), the lithium anode contacting CSIL solid electrolyte after cycling remains smooth, shiny and no distinct lithium dendrites were observed (Figure S17b, Supporting Information). This result indicates that CSIL solid electrolyte effectively inhibit the growth of lithium dendrites. In addition, CSIL electrolyte kept intact and no apparent lithium dendrites were found (Figure S17c,d, Supporting Information). Figure S17e,f (Supporting Information) show LFP after cycling is more homogeneity compared to before cycling and there is no lithium dendrite was observed in the electrode surface after charge/discharge cycling. Taken together, these results elucidate that the CSIL solid electrolyte effectually enhance the lithium-ion transport in batteries, and uniformly distributes the Li<sup>+</sup> on electrode surface. In addition, the cycling performance of CSIL solid electrolyte at 3 C was investigated to determine the lifetime and cycling stability of the batteries functionalized solid electrolyte. It shows the specific capacity of LiBs with CSIL solid electrolyte can work stably for more than 500 cycles with a retention of 90% (Figure 4d). Tables S1 and S2 (Supporting Information) indicate the dominance of our CSIL solid electrolyte compared with UIO-66/Li-IL, UIO-67/Li-IL, and recently reported works based on solid electrolytes. Based on the above results, the excellent electrochemical performance of Li/CSIL/LFP battery makes the novel CSIL solid electrolyte highly promising for room temperature solid-state LiBs.

### 3. Conclusion

In this work, an attempt is performed to utilize a novel UIO-66@67 bifunctional host with lithium ionic liquid (CSIL) as a

solid electrolyte for advanced solid-state LiBs. The fabricated CSIL solid electrolyte can facilitate an enhanced effect in the lithium-ion transport, high ionic conductivity, and low polarization with uniform Li plating/stripping for more than 1000 h under 1000  $\mu\text{A cm}^{-2}$ , at room temperature. The CSIL solid electrolyte exhibited excellent cycling stability with high Coulombic efficiency at room temperature. The CSIL solid electrolyte also demonstrated good compatibility and superior interfacial contact with Li metal anode and LFP cathode. Eventually, it can be inferred that the UIO-66@67 with rational designed with different pore sizes as a host for IL could be extended to other core-shell material for high-performance solid-state LiBs.

## 4. Experimental Section

**Material Preparation:** 1,4-Benzenedicarboxylic acid (99%), biphenyl-4,4-dicarboxylic acid (99%), benzoic acid (99%), acetate (99.7%), and *N,N*-dimethyl formamide (DMF 99%) were purchased from Aladdin. Zirconium(IV) chloride (98%) were purchased from Macklin. EMIM-TFSI (97%) and LiTFSI (97%) were also purchased from Aladdin. Concentrated hydrochloric acid (36–38%) and ethanol absolute, are of analytical grade and used directly without any further purification. The synthesis of UIO-66, UIO-67, and UIO-66@UIO-67 was conducted by solvothermal process

**Material Preparation—Preparation of the UIO-66:** UIO-66 framework was synthesized according to the procedure reported previously.<sup>[63]</sup> In a typical reaction, a Teflon-lined bomb hydrothermal autoclave was loaded with 0.227 mmol (54 mg)  $\text{ZrCl}_4$ , 0.227 mmol (34 mg) terephthalic acids, and 29 mL (24.9 g) DMF. The mixture was sonicated for 20 min to get a homogeneous solution, and the bomb was sealed before being heated at 120 °C for 24 h. After cooling to room temperature followed by centrifugation (10 000 rpm for 5 min) and sequentially washing three times with DMF (3 × 30 mL) and EtOH (3 × 30 mL), the nanocrystalline MOF (UIO-66) was obtained subsequently drying in a vacuum oven at 60 °C. the obtained MOFs were activated at 250 °C for 1 h with heating rate of 1 °C/2 min.

**Material Preparation—Preparation of the UIO-67:** UIO-67 was synthesized with little modification reported elsewhere.<sup>[64]</sup> Briefly, 502 mg  $\text{ZrCl}_4$ , 520 mg  $\text{H}_2$ -bpdcc, and 2.63 g benzoic acid were mixed with 50 mL DMF and 0.152 mL HCl under sonication for 20 min at room temperature. The resultant solution was then transferred into a 100 mL Teflon-lined autoclave and placed in an oven at 120 °C for 48 h. The white precipitates were obtained by centrifugation after cooling to room temperature and followed by washing and drying UIO-67. the obtained MOFs were activated at 250 °C for 1 h with heating rate of 1 °C/2 min.

**Material Preparation—Preparation of the UIO-66@67:** UIO-66@67 were prepared by facile solvothermal process with different linkers.<sup>[65]</sup> Typically, 140 mg UIO-66 powder, 93.2 mg  $\text{ZrCl}_4$ , 97.6 mg  $\text{H}_2$ -bpdcc and 488 mg benzoic acid was dissolved in 0.8 mL acetate and 50 mL DMF at room temperature. The mixture solution was loaded in Teflon lined autoclave after being sonicated for 30 min. The obtained homogeneous solution was sealed and placed in a preheated oven at 120 °C for 24 h. The white color precipitates were collected by centrifugation at 10 000 rpm for 5 min. After successive washing and drying, the obtained MOFs were activated at 250 °C for 1 h with heating rate of 1 °C/2 min.

**Material Preparation—Preparation of the Li-IL@MOF:** For the synthesis of Li-IL@MOF in a typical reaction, LiTFSI (1.395 g) was dissolved in EMIM-TFSI (5 mL) by magnetic stirring at room temperature for 1 h. The resultant solution was heated at 120 °C for overnight to obtain lithium ionic liquid (Li-IL). Different amount of Li-IL was loaded into activated MOF UIO-66, UIO-67 and UIO-66@67 separately, by sufficiently mixing with mortar and pestle until a homogeneous mixture is obtained. The homogeneous mixtures were heated at 120 °C for overnight under vacuum overnight to obtain Li-IL@MOF. Through this process, the

residual guest molecules in the MOF crystals were evacuated from the pores for better Li-IL infiltration.

**Material Preparation—Preparation of the Cathode:** To fabricate the cathode, commercial  $\text{LiFePO}_4$ , CSIL, and black acetylene powder was added subsequently with different ratios to *N*-methyl-2-pyrrolidone (NMP) followed by stirring at room temperature for 12 h until a homogenous mixture is obtained. The resulting slurry was cast onto an aluminum foil and dried under vacuum conditions at 120 °C for 6 h. The active material  $\text{LiFePO}_4$  (LFP) loading in the cathodes was measured to be 2–4  $\text{mg cm}^{-2}$ .

**Material Preparation—Preparation of Li-IL@MOF Solid Electrolyte:** To fabricate the nanostructured Li-IL/UIO solid electrolyte, the obtained core-shell MOFs were heated at 0.5 °C  $\text{min}^{-1}$  to 250 °C with a soaking time of 1 h to evaporate the excess dissolved liquid. In the next step, different amounts of Li-IL were added and blended manually by mortar and pestle before heating at 120 °C for 12 h to achieve better absorption. The solid electrolyte membrane with 15 mm diameter and 160  $\mu\text{m}$  thickness was successfully obtained by pressing into stainless steel mold under a 10 MPa for 2 min between two stainless steel heads.

**Materials Characterization:** The overall morphology and nanostructure were investigated by field emission scanning electron microscope (FSEM JEOL JSM-7100FA) with an acceleration voltage of 20kV. Elemental analysis was performed by the energy-dispersive X-ray spectroscopy (Oxford IE250 system). TEM images were captured and recorded by using JEM-2100F with acceleration voltage 200kV. Crystallographic characterization of different MOFs was conducted by D8 Discover X-ray diffractometer using  $\text{Cu K}\alpha$  X-ray source with radiation ( $\lambda = 1.5418 \text{ \AA}$ ). FT-IR measurements were obtained using Nicolet 6700 (Thermo Fisher Scientific Co., USA) IR spectrometer with a wavenumber range from 400 to 4000  $\text{cm}^{-1}$ . Thermogravimetric analysis (TGA) was performed in the Argon atmosphere from 30 to 700 °C with a heating rate of 10 °C  $\text{min}^{-1}$  using Netzsch STA 449C simultaneous analyzer. The  $\text{N}_2$  adsorption/desorption isothermal was performed by the TriStar-3020 gas adsorption analyzer at 77 K (Micromeritics Instrument Co., USA). The X-ray photoelectron spectroscopy (XPS) analysis was carried out by ESCALAB 250 Xi spectrometer (VG Scientific Co., UK).

**Electrochemical Measurements:** Ionic conductivity of UIO-66, UIO-67, the UIO-66@67 with IL was determined by EIS after placing the electrolyte between two electrodes (stainless steel) contacts in a CR2025 coin cell. A NOVOCONTROL spectrometer system was used for measurements at various temperatures from –10 to 120 °C with a step size of 20 °C and frequency ranges from  $10^6$  to 0.1 Hz and at an amplitude of 100 mV. The bulk resistance of the samples was calculated from the EIS curve. The ionic conductivity was obtained using Equation (1)

$$\sigma = \frac{T}{SR_b} \quad (1)$$

where  $S$  and  $T$  represent the area and thickness of the electrolyte pellets, respectively.  $R_b$  is the bulk resistance and  $\sigma$  is the ionic conductivity ( $\text{S cm}^{-1}$ ). To calculate the activation energies, the ionic conductivity has been measured at different temperatures from –10 to 120 °C and calculated by Arrhenius relation.

The activation energies ( $E_a$ ) of solid electrolytes were calculated according to the Arrhenius relation from Equation (2)<sup>[47]</sup>

$$\sigma = A \exp\left(\frac{E_a}{kT}\right) \quad (2)$$

where  $\sigma$  is ionic conductivity of the solid electrolyte,  $A$  is the pre-exponential factor,  $E_a$  is the activation energy,  $k$  is the Boltzmann constant, and  $T$  is the temperature of the testing process.

The Li-ion transference number ( $t_{\text{Li}^+}$ ) of CSIL solid electrolyte was tested in symmetric lithium cell using a NOVOCONTROL spectrometer system at room temperature by a combination of DC polarization and AC impedance measurement. A DC potential ( $\Delta V = 10 \text{ mV}$ ) was applied for 5500 s to gain the initial and steady currents. Meanwhile, the AC

impedance spectra of the same cell were measured before and after polarization. The value of  $t_{\text{Li}^+}$  has been calculated by Equation (3)

$$t_{\text{Li}^+} = \frac{I_{(t=\infty)}(\Delta V - I_{(t=0)}R_{(t=0)})}{I_{(t=0)}(\Delta V - I_{(t=\infty)}R_{(t=\infty)})} \quad (3)$$

where  $R_{(t=0)}$  and  $R_{(t=\infty)}$  are the AC impedances before and after polarization, respectively,  $I_{(t=0)}$  and  $I_{(t=\infty)}$  are the initial and steady currents, respectively.

The electrochemical stability window (ESW) of CSIL Solid electrolytes was monitored by asymmetric cell (Li/CSIL/SS) via linear sweep voltammetry (LSV) from 0 to 6V at a scan rate 0.5 mV s<sup>-1</sup> at room temperature by using a NOVOCONTROL spectrometer system.

cyclic stability of CSIL solid electrolyte against lithium metals was measured by Li symmetrical cell using a LANHE CT2001A charge/discharge system at different current densities from 100 to 1000 μA cm<sup>-2</sup> at room temperature with 2 h charge/discharge cycles.

The cycle performance and specific capacity of the CSIL solid electrolyte were measured by a full cell (LFP/CSIL/Li) using a LANHE CT2001A charge/discharge system. The cathode was prepared from a slurry composed of LiFePO<sub>4</sub> (MTI), CSIL electrolyte, acetylene black, and 1-methyl-2-pyrrolidinone (NMP, 99.9%, Aladdin). This mixture was stirred for 6 h in order to become homogeneous. Finally, to construct the composite cathode, the obtained slurry was coated on Al foils before being dried at 120 °C by vacuum oven for 7 h.

## Supporting Information

Supporting Information is available from the Wiley Online Library or from the author.

## Acknowledgements

This work was supported by the National Natural Science Foundation of China (51802239), Foshan Xianhu Laboratory of the Advanced Energy Science and Technology Guangdong Laboratory (XHT2020-005, XHT2020-003), the Natural Science Foundation of Hubei Province (2019CFA001), and the Fundamental Research Funds for the Central Universities (WUT:2020111011GX, 20201VB057, 20191VB054, 2019111062JL).

## Conflict of Interest

The authors declare no conflict of interest.

## Author Contributions

A.E.A. and J.S. contributed equally to this work. L.X. and L.M. were in charge of this scientific research project, and the leaders of actual coordination of contributions. A.E.A. performed all the experiments and the data analyses as well as wrote the manuscript. All the authors discussed the data analysis and revised the manuscript.

## Data Availability Statement

Research data are not shared.

## Keywords

bifunctional hosts, core-shell, electrochemical energy storage, lithium-ion batteries

Received: May 31, 2021  
Published online:

- [1] M. S. Dresselhaus, I. L. Thomas, *Nature* **2001**, *414*, 332.
- [2] M. Armand, J. M. Tarascon, *Nature* **2008**, *451*, 652.
- [3] J. B. Goodenough, Y. Kim, *Chem. Mater.* **2010**, *22*, 587.
- [4] M. Safa, A. Chamaani, N. Chawla, B. El-Zahab, *Electrochim. Acta* **2016**, *213*, 587.
- [5] S. Xin, Y. You, S. Wang, H.-C. Gao, Y.-X. Yin, Y.-G. Guo, *ACS Energy Lett.* **2017**, *2*, 1385.
- [6] C. S. Rustomji, Y. Yang, T. K. Kim, J. Mac, Y. J. Kim, E. Caldwell, H. Chung, Y. S. Meng, *Science* **2017**, *356*, eaal4263.
- [7] R. Bouchet, S. Maria, R. Meziane, A. Aboulaich, L. Lienafa, J.-P. Bonnet, T. N. T. Phan, D. Bertin, D. Gigmes, D. Devaux, R. Denoyel, M. Armand, *Nat. Mater.* **2013**, *12*, 452.
- [8] S. Tang, Q. Lan, L. Xu, J. Liang, P. Lou, C. Liu, L. Mai, Y.-C. Cao, S. Cheng, *Nano Energy* **2020**, *71*, 104600.
- [9] Z. Gao, H. Sun, L. Fu, F. Ye, Y. Zhang, W. Luo, Y. Huang, *Adv. Mater.* **2018**, *30*, 1705702.
- [10] J. Janek, W. G. Zeier, *Nat. Energy* **2016**, *1*, 16141.
- [11] Z. Zhang, Y. Shao, B. Lotsch, Y.-S. Hu, H. Li, J. Janek, L. F. Nazar, C.-W. Nan, J. Maier, M. Armand, L. Chen, *Energy Environ. Sci.* **2018**, *11*, 1945.
- [12] Q. Zhang, K. Liu, F. Ding, X. Liu, *Nano Res.* **2017**, *10*, 4139.
- [13] J. C. Bachman, S. Muy, A. Grimaud, H.-H. Chang, N. Pour, S. F. Lux, O. Paschos, F. Maglia, S. Lupart, P. Lamp, L. Giordano, Y. Shao-Horn, *Chem. Rev.* **2016**, *116*, 140.
- [14] A. Manthiram, X. Yu, S. Wang, *Nat. Rev. Mater.* **2017**, *2*, 16103.
- [15] Z. Stoeva, I. Martin-Litas, E. Staunton, Y. G. Andreev, P. G. Bruce, *J. Am. Chem. Soc.* **2003**, *125*, 4619.
- [16] B. Scrosati, *Chem. Rec.* **2005**, *5*, 286.
- [17] F. Zheng, M. Kotobuki, S. Song, M. O. Lai, L. Lu, *J. Power Sources* **2018**, *389*, 198.
- [18] N. Kamaya, K. Homma, Y. Yamakawa, M. Hirayama, R. Kanno, M. Yonemura, T. Kamiyama, Y. Kato, S. Hama, K. Kawamoto, A. Mitsui, *Nat. Mater.* **2011**, *10*, 682.
- [19] D. Y. Oh, Y. J. Nam, K. H. Park, S. H. Jung, S.-J. Cho, Y. K. Kim, Y.-G. Lee, S.-Y. Lee, Y. S. Jung, *Adv. Energy Mater.* **2015**, *5*, 1500865.
- [20] S. Wenzel, S. Randau, T. Leichtweiß, D. A. Weber, J. Sann, W. G. Zeier, J. Janek, *Chem. Mater.* **2016**, *28*, 2400.
- [21] Y. Kato, S. Hori, T. Saito, K. Suzuki, M. Hirayama, A. Mitsui, M. Yonemura, H. Iba, R. Kanno, *Nat. Energy* **2016**, *1*, 16030.
- [22] L. Fan, S. Wei, S. Li, Q. Li, Y. Lu, *Adv. Energy Mater.* **2018**, *8*, 1702657.
- [23] S. Wang, Q. Bai, A. M. Nolan, Y. Liu, S. Gong, Q. Sun, Y. Mo, *Angew. Chem., Int. Ed.* **2019**, *58*, 8039.
- [24] Y. Zhang, T.-T. Zuo, J. Popovic, K. Lim, Y.-X. Yin, J. Maier, Y.-G. Guo, *Mater. Today* **2020**, *33*, 56.
- [25] C. W. Liew, R. Durairaj, S. Ramesh, *PLoS One* **2014**, *9*, e102815.
- [26] J. Y. Song, Y. Y. Wang, C. C. Wan, *J. Power Sources* **1999**, *77*, 183.
- [27] W. H. Meyer, *Adv. Mater.* **1998**, *10*, 439.
- [28] Z. Wan, D. Lei, W. Yang, C. Liu, K. Shi, X. Hao, L. Shen, W. Lv, B. Li, Q.-H. Yang, F. Kang, Y.-B. He, *Adv. Funct. Mater.* **2019**, *29*, 1805301.
- [29] S. Yu, S. Schmohl, Z. Liu, M. Hoffmeyer, N. Schön, F. Hausen, H. Tempel, H. Kungl, H. D. Wiemhöfer, R. A. Eichel, *J. Mater. Chem. A* **2019**, *7*, 3882.
- [30] L. Liu, L. Chu, B. Jiang, M. Li, *Solid State Ionics* **2019**, *331*, 89.
- [31] P. Horcajada, C. Serre, M. Vallet-Regí, M. Sebban, F. Taulelle, G. Férey, *Angew. Chem., Int. Ed.* **2006**, *45*, 5974.



- [32] L. J. Murray, M. Dincă, J. R. Long, *Chem. Soc. Rev.* **2009**, *38*, 1294.
- [33] J. An, S. J. Geib, N. L. Rosi, *J. Am. Chem. Soc.* **2010**, *132*, 38.
- [34] C. A. Kent, B. P. Mehl, L. Ma, J. M. Papanikolas, T. J. Meyer, W. Lin, *J. Am. Chem. Soc.* **2010**, *132*, 12767.
- [35] O. K. Farha, A. M. Shultz, A. A. Sarjeant, S. T. Nguyen, J. T. Hupp, *J. Am. Chem. Soc.* **2011**, *133*, 5652.
- [36] L. E. Kreno, K. Leong, O. K. Farha, M. Allendorf, R. P. Van Duyne, J. T. Hupp, *Chem. Rev.* **2012**, *112*, 1105.
- [37] A. Banerjee, U. Singh, V. Aravindan, M. Srinivasan, S. Ogale, *Nano Energy* **2013**, *2*, 1158.
- [38] R. Wu, X. Qian, X. Rui, H. Liu, B. Yadian, K. Zhou, J. Wei, Q. Yan, X.-Q. Feng, Y. Long, L. Wang, Y. Huang, *Small* **2014**, *10*, 1932.
- [39] F. Zou, X. Hu, Z. Li, L. Qie, C. Hu, R. Zeng, Y. Jiang, Y. Huang, *Adv. Mater.* **2014**, *26*, 6622.
- [40] G. Zhang, S. Hou, H. Zhang, W. Zeng, F. Yan, C. C. Li, H. Duan, *Adv. Mater.* **2015**, *27*, 2400.
- [41] M. Nagarathinam, K. Saravanan, E. J. H. Phua, M. V. Reddy, B. V. R. Chowdari, J. J. Vittal, *Angew. Chem., Int. Ed.* **2012**, *51*, 5866.
- [42] J. Tang, R. R. Salunkhe, J. Liu, N. L. Torad, M. Imura, S. Furukawa, Y. Yamauchi, *J. Am. Chem. Soc.* **2015**, *137*, 1572.
- [43] J. Liu, C. Wu, D. Xiao, P. Kopold, L. Gu, P. A. van Aken, J. Maier, Y. Yu, *Small* **2016**, *12*, 2354.
- [44] H. Furukawa, N. Ko, Y. B. Go, N. Aratani, S. B. Choi, E. Choi, A. Ö. Yazaydin, R. Q. Snurr, M. O'Keeffe, J. Kim, O. M. Yaghi, *Science* **2010**, *329*, 424.
- [45] N. Chen, Y. Li, Y. Dai, W. Qu, Y. Xing, Y. Ye, Z. Wen, C. Guo, F. Wu, R. Chen, *J. Mater. Chem. A* **2019**, *7*, 9530.
- [46] R. Zhao, Z. Liang, R. Zou, Q. Xu, *Joule* **2018**, *2*, 2235.
- [47] Y. Xia, N. Xu, L. Du, Y. Cheng, S. Lei, S. Li, X. Liao, W. Shi, L. Xu, L. Mai, *ACS Appl. Mater. Interfaces* **2020**, *12*, 22930.
- [48] L. Shen, H. B. Wu, F. Liu, J. L. Brosmer, G. Shen, X. Wang, J. I. Zink, Q. Xiao, M. Cai, G. Wang, Y. Lu, B. Dunn, *Adv. Mater.* **2018**, *30*, 1707476.
- [49] B. M. Wiers, M.-L. Foo, N. P. Balsara, J. R. Long, *J. Am. Chem. Soc.* **2011**, *133*, 14522.
- [50] C. Gerbaldi, J. R. Nair, M. A. Kulandainathan, R. S. Kumar, C. Ferrara, P. Mustarelli, A. M. Stephan, *J. Mater. Chem. A* **2014**, *2*, 9948.
- [51] R. Senthil Kumar, M. Raja, M. Anbu Kulandainathan, A. Manuel Stephan, *RSC Adv.* **2014**, *4*, 26171.
- [52] Z. Wang, Z. Wang, L. Yang, H. Wang, Y. Song, L. Han, K. Yang, J. Hu, H. Chen, F. Pan, *Nano Energy* **2018**, *49*, 580.
- [53] Z. Wang, R. Tan, H. Wang, L. Yang, J. Hu, H. Chen, F. Pan, *Adv. Mater.* **2018**, *30*, 1704436.
- [54] J.-F. Wu, X. Guo, *Small* **2019**, *15*, 1804413.
- [55] K. Fujie, R. Ikeda, K. Otsubo, T. Yamada, H. Kitagawa, *Chem. Mater.* **2015**, *27*, 7355.
- [56] Q. Ma, X. Qi, B. Tong, Y. Zheng, W. Feng, J. Nie, Y.-S. Hu, H. Li, X. Huang, L. Chen, Z. Zhou, *ACS Appl. Mater. Interfaces* **2016**, *8*, 29705.
- [57] D. Zhou, R. Liu, J. Zhang, X. Qi, Y.-B. He, B. Li, Q.-H. Yang, Y.-S. Hu, F. Kang, *Nano Energy* **2017**, *33*, 45.
- [58] Z. Wang, S. Wang, A. Wang, X. Liu, J. Chen, Q. Zeng, L. Zhang, W. Liu, L. Zhang, *J. Mater. Chem. A* **2018**, *6*, 17227.
- [59] W. Xu, X. Pei, C. S. Diercks, H. Lyu, Z. Ji, O. M. Yaghi, *J. Am. Chem. Soc.* **2019**, *141*, 17522.
- [60] S. S. Park, Y. Tulchinsky, M. Dincă, *J. Am. Chem. Soc.* **2017**, *139*, 13260.
- [61] C. Largeot, C. Portet, J. Chmiola, P.-L. Taberna, Y. Gogotsi, P. Simon, *J. Am. Chem. Soc.* **2008**, *130*, 2730.
- [62] G. Wang, P. He, L.-Z. Fan, *Adv. Funct. Mater.* **2020**, *31*, 2007198.
- [63] J. H. Cavka, S. Jakobsen, U. Olsbye, N. Guillou, C. Lamberti, S. Bordiga, K. P. Lillerud, *J. Am. Chem. Soc.* **2008**, *130*, 13850.
- [64] S. Øien-Ødegaard, B. Bouchevreau, K. Hylland, L. Wu, R. Blom, C. Grande, U. Olsbye, M. Tilset, K. P. Lillerud, *Inorg. Chem.* **2016**, *55*, 1986.
- [65] Y. Gong, Y. Yuan, C. Chen, P. Zhang, J. Wang, S. Zhuiykov, S. Chaemchuen, F. Verpoort, *J. Catal.* **2019**, *371*, 106.